Original Research Article

aeroacoustics

International Journal of Aeroacoustics
2021, Vol. 0(0) 1–31

DOI: 10.1177/1475472X211052699
journals.sagepub.com/home/jae
SAGE

Fundamental investigation using active plasma control to reduce blade–vortex interaction noise

Trushant K Patel[1], Alexander J Lilley[1], Weiqi Shen[1], Christian Porrello[2], Alexander Schindler-Tyka[2], Subrata Roy[1,2], William E Lear[2], and Steven AE Miller[1]

Abstract

Blade vortex interaction noise is a problematic and dominant component of rotor noise. Plasma actuators strategically placed at the tip of the rotor blades can reduce the strength of the tip vortices. This reduction has the potential to significantly reduce blade vortex interaction noise. A combined experimental, numerical, and theoretical program shows supporting evidence that low power plasma actuators can effectively lower coherence of the blade tip vortex and reduce blade vortex interaction noise over-pressure by up to 80%. For a nominal small five-bladed unmanned aerial vehicle, we predict an approximate 8.88 maximum ΔdB reduction for a 150 m/s tip speed. Experimental, computational, and acoustic modeling support these predictions. This study represents a fundamental investigation in the fixed-frame, which provides evidence for higher level research and testing in a rotating framework.

Keywords

Flow-control, noise, plasma actuator, rotor, blade vortex interaction

Date received: 13 October 2021; revised: 14 August 2021; accepted: 14 August 2021

Introduction

The noise from rotorcraft has been an on-going source of community annoyance and detectability vector for military applications for decades. Newly developed urban air mobility (UAM) and distributed electric propulsion (DEP) concepts also have community annoyance and acceptance

---

[1]University of Florida, Gainesville, FL, USA
[2]SurfPlasma, INC., Gainesville, FL, USA

Corresponding author:
Steven AE Miller, University of Florida, Department of Mechanical and Aerospace Engineering, PO BOX 116250, Gainesville, FL 32611, USA.
Email: saem@ufl.edu

challenges. During particular maneuvers or descent operations, the wake and tip vortices from one blade might impinge on a proceeding blade. This turbulent breakup of the tip vorticity causes periodic broadband noise, which is one of the dominant types of noise from rotorcraft. This type of acoustic source of rotorcraft is called blade vortex interaction (BVI) noise (see Schlinker and Amiet[1]). This paper presents basic research to ascertain the feasibility of using plasma actuators to reduce the strength of rotor tip vorticities for the purpose of reducing BVI noise.

We investigate the feasibility of a new reduction technology for BVI noise through a fundamental research program. Plasma actuators have been shown to control flow fields.[2–5] We place plasma actuators at strategic locations at the blade tip to reduce the strength of the tip vortex. These actuators in turn reduce the strength of the tip vorticity. They also have the effect of slightly redirecting the tip vortex and slightly altering its core radius. The purpose of this paper is to show that plasma actuators, which use a very small amount of energy, can alter the vortex strength. We then predict flow-field quantities with computational fluid dynamics (CFD) and wind tunnel experiments to inform a validated BVI noise model. This model predicts lowered BVI noise through our presently proven plasma actuators and destruction of the blade tip vortex.

Reduction of BVI noise in communities benefits physical health,[6–9] reduces human annoyance near air-portals,[10] and reduces community mental health issues.[11] Clearly, the reduction of BVI noise in traditional helicopters or future vertical take-off and landing (vTOL) vehicles that are tightly integrated in communities will benefit society. If vTOL are to be integrated into communities, then BVI noise must be reduced for acceptance, and this methodology is one avenue forward. Plasma actuation, which uses low energy and nearly no modification of rotor blades, can lead to greatly reduced annoyance and reduced noise related health effects in communities. It is important to note that there is a significant concern for ozone produced from plasma actuators in quiescent industrial environment. Both OSHA and NIOSH set an admissible limit of 0.1 ppm for an 8 h per day human exposure. While plasma actuators can produce copious amounts of ozone (exceeding 200 ppm[12]), its highest concentration remains within a few centimeters of the actuator surface. Our application is in an open air environment, where the ozone concentration exponentially decays with distance and time. Especially during take-off and landing conditions, high air exchange rates are expected to reduce the ozone concentration very quickly to within the acceptable OSHA limit.

The BVI noise is mainly dependent on the vortex strength, miss distance, that is, the separation distance of the vortex from the airfoil, and the length of the interaction of the vortex with the airfoil. Many different noise reduction techniques have been explored,[13–23] which include addition of porous surfaces, active flap control, tapered segments and flaps, trim strategies, and higher harmonic pitch control. Most of the noise reduction methods increase the miss distance by actively controlling the rotor pitch and flaps or reduce the interaction length between the vortex and airfoil using porous surfaces. Lee[18] used porous surfaces on the leading edge of the airfoil to reduce the transpiration pressure due to BVI and observed a maximum reduction of 30% amplitude of BVI noise. The reduction of noise through miss distance has been investigated by multiple researchers using higher harmonic control,[21,23] hub pitching moment,[24] active twist rotor,[20] etc. A maximum reduction of 6 to 7 dB has been observed using these methods. However, in the present work, we use plasma actuators to directly reduce the vortex strength, and thereby, reduce the BVI noise.

Prediction techniques[25–33] vary from semi-empirical models to expensive CFD calculations. BVI noise physics and illustrations are shown for one vortex interaction during descent in Tangler.[34] The acoustic pressure-time history of one such BVI event is shown in Malpica et al.[19,24] The BVI noise is dependent on the vortex strength, Γ, which we intend to reduce through plasma actuation. This concept is inspired by Schmitz[15] in his work on x-force control, which is essentially a force balance to alter and reduce BVI rotor surface in the 80% to 100% span range. This concept has previously been explored during the Boeing Smart Material Actuated Rotor Technology (SMART) test with active trailing-edge flaps[35] in the National Full-Scale Aerodynamics Complex (NFAC) 40-ft-by-80-ft wind tunnel at NASA Ames Research Center.

Plasma actuators are active devices that have been demonstrated to control boundary layers via electromagnetic body forces, including formation of vortices. Our approach is to incorporate plasma actuators near the tip of the blades to reduce noise and maintain performance. Plasma actuation has been used for aerodynamic noise control previously.[36–38] Recent research[39] has shown that for certain positioning and for a voltage-frequency combination, the streamwise plasma vortex generators are effective in suppressing the vortex shedding tonal noise (as well as the mean and turbulent drag). For example, using a relatively low input voltage of 3.0 kV for the streamwise vortex generating plasma actuators, a 4 to 12 dB tonal noise reduction was achieved via inducing only about 7% of the freestream velocity. Here, we develop dielectric barrier discharge (DBD) serpentine and fan plasma actuators for the purpose of reducing the strength of tip vorticities. These will be effective during large adverse pressure gradients that are typical during take-off, landing, and maneuvers of rotorcraft.

The serpentine plasma actuator, originally introduced by Roy and Wang[3] to modify boundary layer thickness, is a lightweight, non-mechanical, surface compliant, active aerodynamic flow control device. It is comprised of two thin metal electrodes shaped in a wavy or comb like pattern separated by a thin dielectric barrier. A schematic of the side view of a serpentine actuator is shown in Figure 1(a), where the powered (top) and grounded (bottom) electrodes are shown in orange. Plasma discharge is highlighted on the top surface of the actuator. Top-down views are shown in Figure 1(c)–(f), and a low-light photograph of an “ignited” or turned-on circular serpentine actuator is shown in Figure 1(g).

The serpentine plasma actuator[3] creates three-dimensional perturbations that exploit the natural behavior of the flow to increase flow control authority. Three-dimensional perturbations take the form of streamwise vortices and twisted vectored jets. They eventually evolve into coherent turbulent boundary layer streaks. The induced vertical velocity component near the plasma region is found to be proportional to the actuator wavelength, and depending on the applied voltage and frequency, can reach upwards of 5 m/s in a quiescent environment. The serpentine designs were also shown to be more effective at generating streamwise and spanwise vorticity than the standard linear

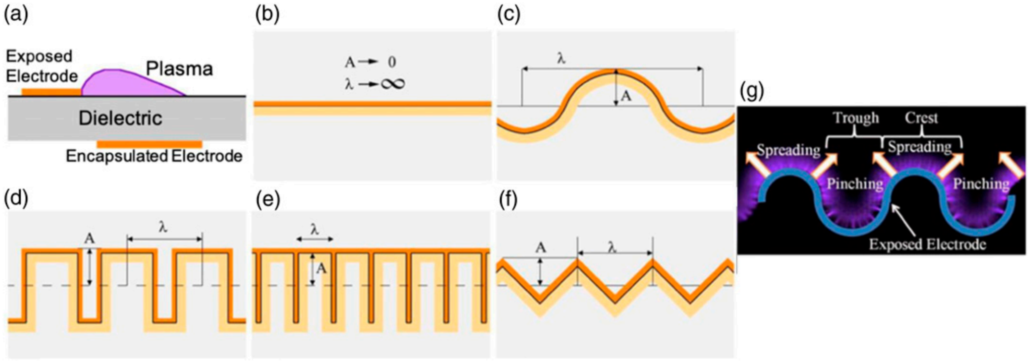

Figure 1. (a) Plasma actuator and the generated body force. (b) Linear actuator. (c)–(f) Serpentine actuators of various geometries: (c) circular, (d) rectangle, (e) comb, (f) triangular, and (g) Ignited circular serpentine actuator.[40]

DBD actuator design.[5] The comb serpentine plasma actuators, which were tuned to flow streaks, were studied for the control of the wake region behind the trailer of a truck.[41]

We also use fan plasma actuators, which are very effective for our application of reducing the strength of wing tip vortices. The fan actuator[42] is a novel surface complaint DBD reactor design. Its purpose is to produce a fully three-dimensional flow that can be designed to selectively introduce opposing vorticity. Its name is derived from the geometrical shape of the electrodes that resemble the blades of a fan. Figure 2 shows the visualization of the swirling flow generated by the "digital fan." In this research effort, the fan actuators aligned near the tip of the blade on the pressure side are most effective at reducing vortex strength.

The paper is organized as follows. First, we present our overall program objectives and methodology. We describe our experimental facility and setup, our computational methods, and the modification of an existing noise model. Results are then presented for the experiments with plasma actuation, numerical results from CFD, and finally, predictions of BVI noise with and without actuation.

Technical approach

Our approach is to incorporate plasma actuators on the surface of the rotors near their tips. We seek to reduce vortex strength via plasma actuation at the rotor tips thereby reducing BVI noise. These electrohydrodynamic forces, generated by plasma actuators on the rotors, provide a practical and controllable means for noise suppression over a range of operating conditions. Our primary goal is to show the feasibility of such an approach in a rotating framework using a simplified experiment of a rotor mounted in a wind tunnel.

We focus on three efforts to show potential BVI noise reduction via plasma actuation. The first involves an experimental program. We fabricate an HH-02 airfoil within the test section. Fan and serpentine actuators are mounted at strategic locations near the tip of the airfoil. We implemented a surface compliant serpentine and fan shaped plasma actuated vortex generators on receptive locations to modify the neighboring flow structures. These are individually actuated within a small wind tunnel with a 8.25 inch by 8.25 inch cross-section test section while the airfoil is mounted on the side. Wind tunnel velocities are varied at low speeds with and without plasma actuation. As BVI noise is primarily dependent on the properties of the tip vortex, we seek to ascertain how these properties change with and without actuation. These properties include the direction, radius, and

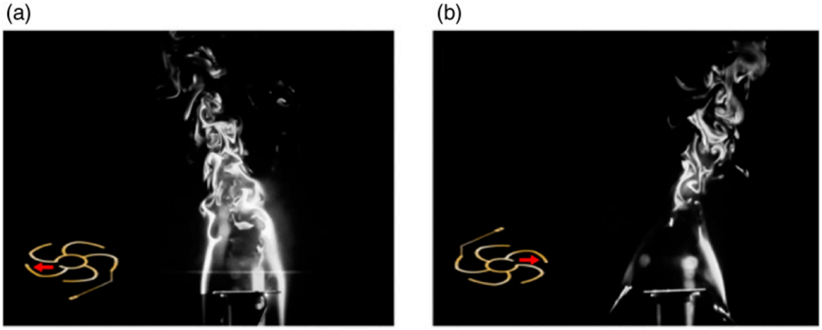

Figure 2. Smoke flow visualization from fan actuator. (a) Opening of the center arc oriented to the left of the image and to the (b) right of the image.[12]

strength of the vortex, which are arguments of the BVI noise model. For this purpose, we perform smoke visualization measurements of the tip vortex downstream from the airfoil at 0.10 and 0.40 chord, c, lengths in conjunction with a high-speed camera. We also perform particle image velocimetry (PIV) measurements of the flow field. The power consumption is recorded for all cases, as it is an important metric for systems.

The second major effort consists of performing CFD simulations of the wind tunnel experiment with and without actuation of the serpentine and fan plasma actuators. These numerical simulations support the noise predictions at low speeds and at moderate speeds near 150 m/s and higher, where wind-tunnel data is not available. These simulations are also used to study how the tip vorticities change with a numerical actuation model, which are compared with the measurements for validation purposes.

The third major effort involved is predicting BVI noise from the wind tunnel experiments and CFD simulations. For this purpose, we modify the BVI noise model of Greenwood et al.[43,44] with a modified vortex strength model, dependent on the plasma actuators and given flight conditions. BVI noise is most sensitive to the vortex strength, Γ, its radius, and its path through the rotor. It is also dependent on the vehicle and its flight path. We validate our implementation of the model with the full-scale experimental measurements from a UH-1H helicopter by Boxwell and Schmitz.[45] BVI predictions are made both in the time-domain and on a ΔdB overall sound pressure level (OASPL) basis on a hemisphere for various tip velocities of a five bladed rotor.

A flowchart of the technical approach to predict the BVI noise using a combination of experimental, computational, and analytical approaches is shown in Figure 3. The influence of the BVI events and resulting noise levels are dependent on the vortex strength, vortex radius, loading pressure on the airfoil blades, and the position where vortices impinge on the proceeding blade. A combination of experimental measurements and CFD simulation data are used as inputs to the BVI noise model. The strength of the vortex and its alteration due to plasma actuators is directly obtained

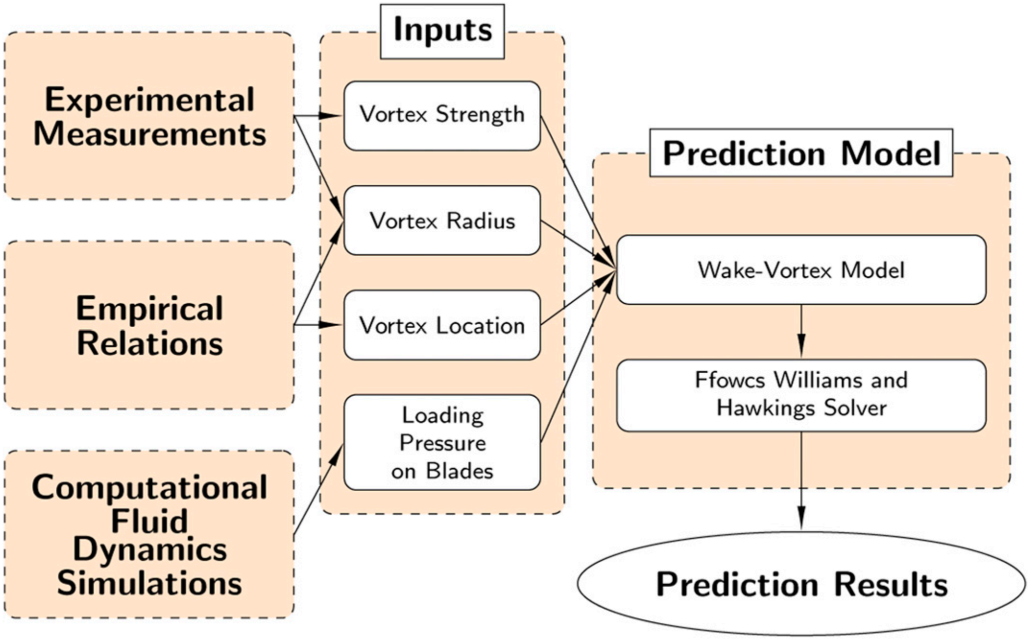

Figure 3. Flowchart of the technical approach.

from the experimental measurements. The pressure loading on the blades is obtained from the CFD simulation results. The initial vortex size and its growth rate control the radius of the vortex core and are estimated using the work of Moore and Saffman.[46] We use the Biot–Savart law[47] to calculate the induced velocity on the blades due to the tip vortex using the path, radius, and strength of the vortex. The induced pressure loading due to the tip vortices is combined with the base pressure loading obtained from CFD simulations. A Ffowcs Williams and Hawkings (FWH) solver[48] is then used to calculate the acoustic pressure at the observer location.

Experimental - Fabrication

The chosen proprietary woven glass reinforced hydrocarbon/ceramic dielectric material of relative dielectric constant 3.7 and thickness of approximately 1 mm allow the actuators to easily bend around the modest radius of curvature found across the midsection of the airfoil. Electrodes are broken up into segments with an average wavelength of 400 wall units and 3 mm gap in between, and are connected to power in parallel. Actuators are printed with a circuit board design software. This type of software can export the actuator design instructions in Gerber format. The Gerber format allows circuit manufacturers to easily manufacture the design. Plated through holes are requested from the manufacturer so that all electrodes can be wired from the unexposed face of the actuator. The copper electrodes are coated with a tin lead coating to better resist corrosion. The actuators are attached to an airfoil that is one foot in chord and corresponds to the HH-02 coordinates. The airfoil is manufactured with a three-dimensional printer. Figure 4 shows the airfoil with plasma glow for the serpentine and fan actuators (top), locations for attaching the actuator plates on the model airfoil (middle), and a representative voltage-current plot with discharge spikes for generating the plasma (bottom).

Experimental - Electronic setup

The fan and plasma actuators require an electric current from a function generator and amplifier. For this purpose, a Tektronix function generator (Model AFG3022B), as shown in Figure 5, is used as input to a Trek 30/20 amplifier. The output of the Trek 30/20 amplifier is measured using a current and voltage probe, which are connected to a Tektronix DPO2014 oscilloscope. The function generator passes a sinusoidal signal to the amplifier. The amplifier output is measured with the

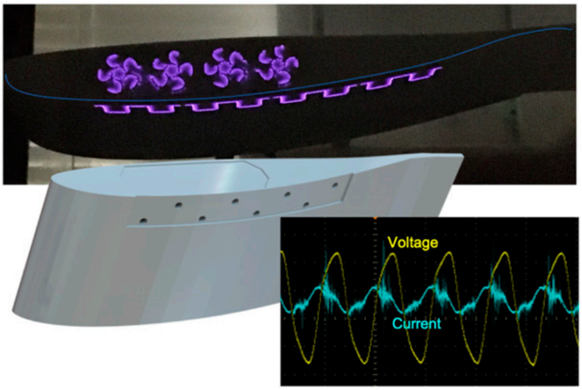

Figure 4. The model airfoil with fan and serpentine plasma actuators turned on during a wind tunnel testing.

voltage and current probes. The output of the probes is read and recorded using the oscilloscope. The oscilloscope is used to determine the voltage, current, and frequency of the sinusoidal signal that is applied to the actuators. Both actuators are used concurrently for all tests. The power consumption of the actuators for each case can be seen in Table 1. The formation of plasmas on the fan and the serpentine actuators are visible to the naked eye.

Experimental - Particle tracking

Wind tunnel experiments are conducted at the Applied Physics Research Group (APRG). The test section has a constant cross-sectional area of 8.25 inches by 8.25 inches and a length of 24 inches with turbulence intensity of 1%. For this particular experiment, the wind tunnel is run at 15 m/s and 35 m/s. The relative humidity is 70%, and the temperature is 294 K. The HH-02 airfoil is mounted on the test section wall, and the tip resides within the middle of the tunnel test section. The wing is set at a constant angle of attack, α, of 4°. The low pressure surface of the airfoil faces the top of the test section. Due to the size of the tunnel and for the interest of examining the dynamics of the tip vortices, we place the trailing edge of the airfoil upstream as possible within the wind tunnel. Therefore, the leading edge of HH-02 airfoil is 0.50 inches from the beginning of the test section.

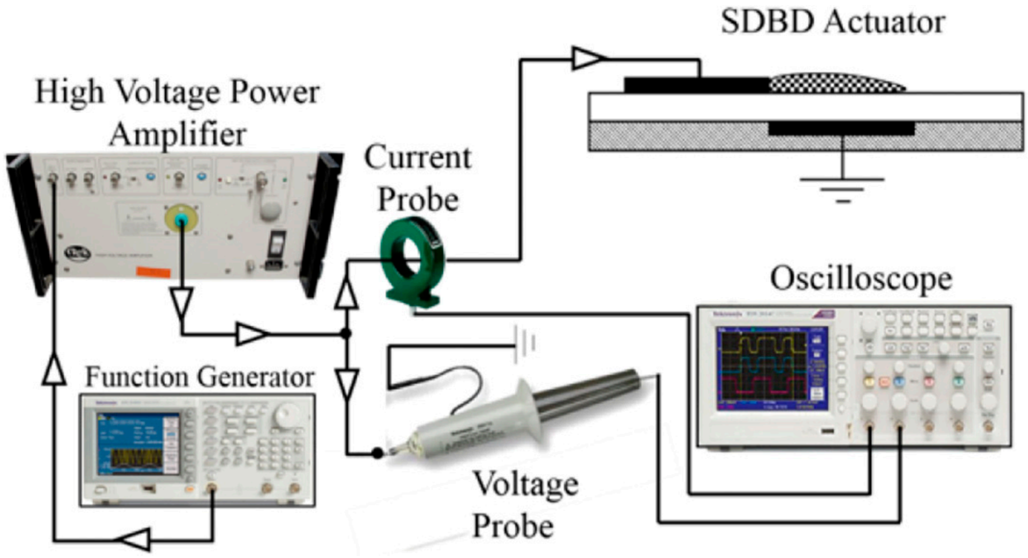

Figure 5. Electrical setup for measurements.

Table 1. Power consumption.

Free-stream velocity, m/s	Voltage, kVpp	Frequency, Hz	Power, W
15	9000	8000	6.41
35	11,000	3000	4.10
35	13,000	2000	6.56
35	13,000	3000	6.89

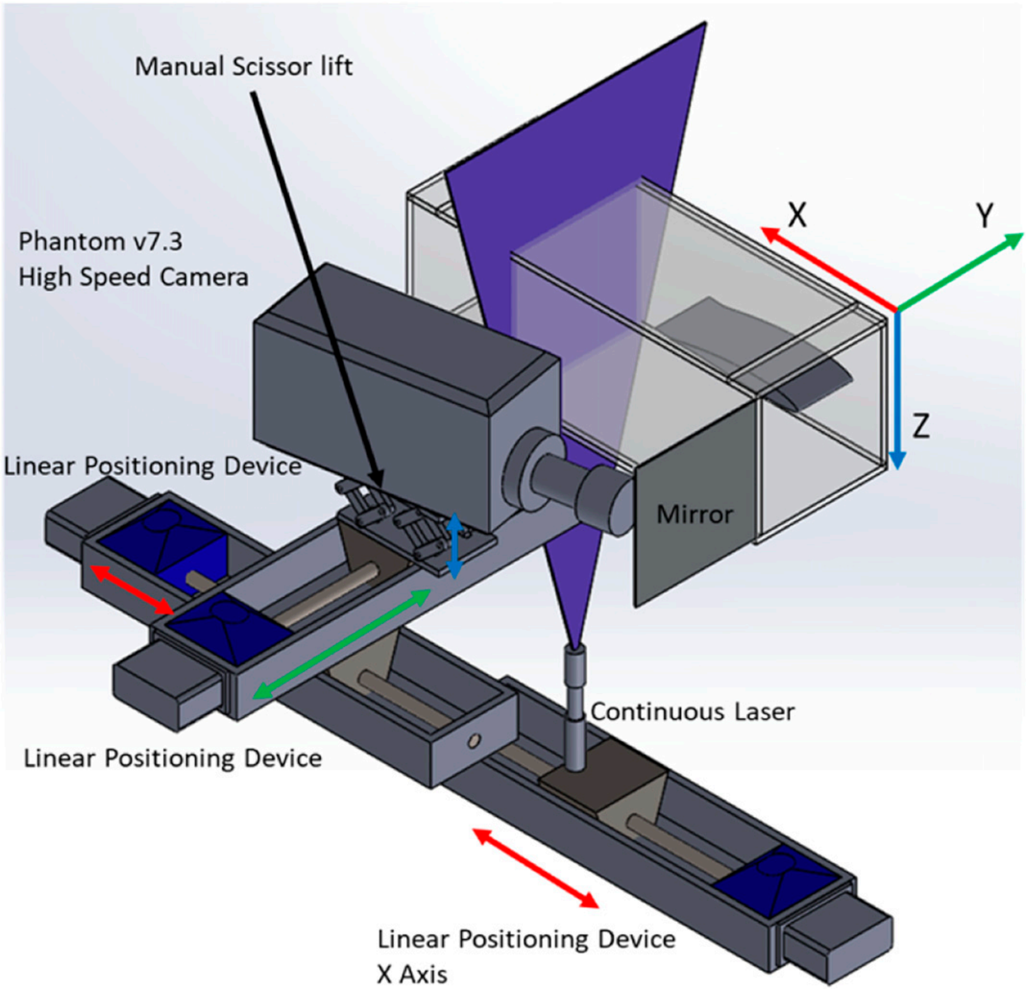

Figure 6. Camera positioning for flow visualization within the wind tunnel.

An 8 Watt 465 nm wavelength continuous blue laser is mounted underneath the test section as shown in Figure 6. A cylindrical concave–convex lens is used to split the beam to a plane with a spreading angle of 20°. The laser plane is located 0.4 chord lengths, 0.4*c*, downstream from the trailing edge of the wing. A water–glycerine mixture fog is used to seed the wind tunnel. The fog generation machine is positioned such that nearly all of the fog is initially on the high-pressure side of the wing. The camera is mounted on two Velmex BiSlides (computer controlled linear positioning devices), which are mounted to an optical table. A manually operated scissor lift is used to add a vertical axis of mobility to the camera. The high-speed camera (Phantom v7.3) is at a slight angle pointed into a mirror. This allows for the focal plane to be larger as the distance is increased between the camera and the focal plane.

In order to quantify changes in vortex strength due to plasma actuation, the circulation, Γ, is calculated. To calculate Γ, the velocity field in the z–y (spanwise plane) is measured via particle image velocimetry. We observe the z–y plane at the 0.4 chord, c, (5 in.) downstream from the trailing edge. The streamwise vorticity, ω_x, is calculated using the u and v velocity components. The circulation, Γ, is defined as

$$\Gamma = \iint \omega_x dS \tag{1}$$

where S is the domain, dS is the area occupied by each point where vorticity is evaluated, and ω_x is the component of the vorticity in the streamwise direction. It is found that the highest frame rate that produced acceptable particles was 12,000 frames per second. A total of 14,438 images are taken, which corresponds to approximately 3.53 s. The resolution of each frame is 416 × 400 pixels. We use the PIVLab software, a free MATLAB toolbox developed by Thielecke,[49] for performing two-dimensional particle image velocimetry calculations.

To identify the vortex region, we evaluate the integral only over regions where Q criterion is positive and the vorticity is negative. The Q criterion is

$$Q = \frac{1}{2}\left(\left|\frac{1}{2}\left(\frac{\partial u_i}{\partial x_j} - \frac{\partial u_j}{\partial x_i}\right)\right|^2 - \left|\frac{1}{2}\left(\frac{\partial u_i}{\partial x_j} + \frac{\partial u_j}{\partial x_i}\right)\right|^2\right) \tag{2}$$

where $\boldsymbol{u}$ is the velocity vector and $\boldsymbol{x}$ is the spatial location vector. As only the velocity components in the spanwise direction are obtained, the circulation and Q criterion are only calculated on the $z-y$ two-dimensional plane.

Computational fluid dynamics

We now describe the computational approach that is used to find both aerodynamic and vortex data for the noise model. Numerical simulations are performed with the ANSYS FLUENT CFD solver.[50] To capture the wingtip vortices, we solved the density-based compressible Reynolds-averaged

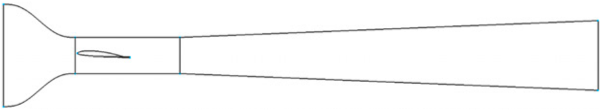

Figure 7. Diagram of the computational domain.

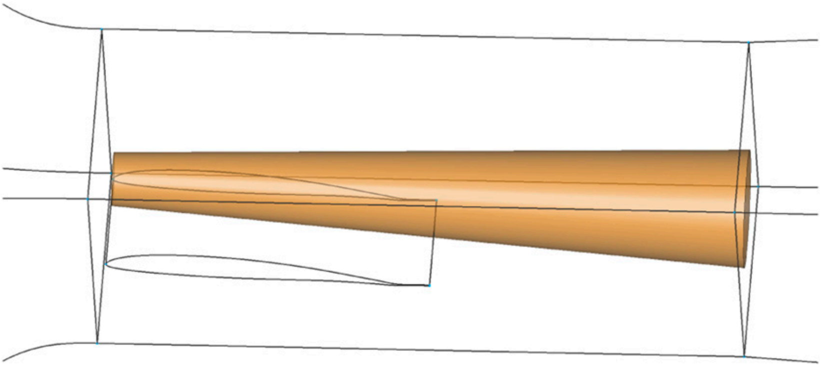

Figure 8. Source zone for mesh refinement.

Navier–Stokes (RANS) equations closed by the Menter $k - \omega$ shear stress transport (SST) turbulence model. A steady state simulation is performed with implicit formulation. The 3rd order MUSCL scheme is used for the spatial discretization of both flow variables and turbulent variables. The AUSM Riemann solver is used for the calculation of interface fluxes.

The computational domain, shown in Figure 7, includes both the wind tunnel and the HH-02 airfoil mounted at the test section location. The computational domain includes the contraction, test section, and the diffuser while the wind tunnel entrance is not modeled to save computational expense. The airfoil is installed 0.5 inches from the inlet of the test section with an angle of attack of 4° to reproduce the experiment. The inlet of the tunnel is located 52.47 inches upstream of the test section. In the downstream of the test section, a diffuser is extended to 95.86 inches to decelerate the flow.

The computational grid refinement within the tip vortex wake is shown in Figure 8. To resolve the wingtip vortex, a source zone is placed in the area where the wingtip vortex is expected. Mesh elements within this zone are isotropically refined with an edge length no larger than 0.2032 cm. The refinement parameters are chosen so that the element size in the refinement zone is of the same order as that near the airfoil surface. The source zone is outlined and shown in Figure 8. On the airfoil, the height of the first cells off the wall are $y^+ = 1$ to resolve the turbulent boundary layer. We note that the limitations in the CFD simulations between the flows with and without actuators are the same as we are comparing alterations of meanflow with and without forcing.

CFD simulations are performed with the actuator on the airfoil "on" and "off." The common mesh parameters for both simulations are listed in Table 2, where grid point spacing is specified in the contraction, test section, diffuser, and airfoil surface. In the CFD simulations, plasma actuators are modeled with body forces in locations and directions that correspond to the physical actuators of

Table 2. Mesh parameters.

Δx_{con} (cm)	Δx_{test} (cm)	Δx_{wing} (cm)	Δx_{diff} (cm)	Δy (cm)	y^+
1.78–1.04	1.04–1.27	0.05–0.13	1.27–8.13	1.27×10^{-3}	1

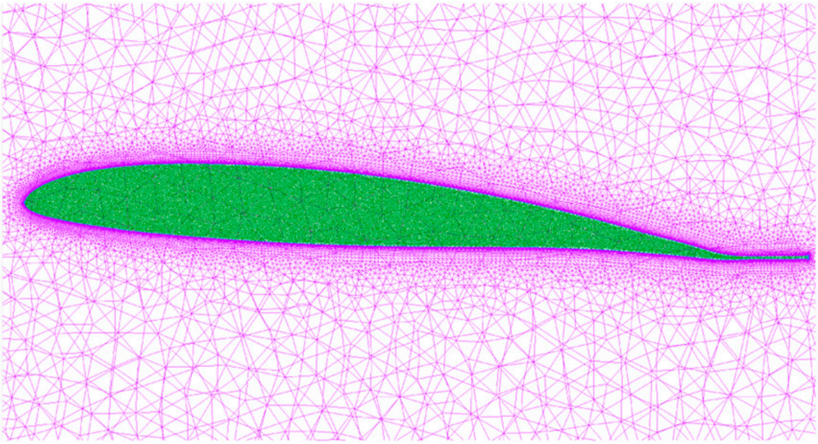

Figure 9. Computational grid on the surface and edge plane of the HH-02 airfoil.

the wind tunnel tests. For the simulation with actuation, an extra constraint on the edge length of elements on the airfoil surfaces are imposed, such that they are able to capture the distribution of the body force due to the actuators. The total number of mesh elements for the actuated and unactuated cases are 4.2 million and 6.5 million, respectively. The final computational mesh on the surface of the HH-02 airfoil is shown in Figure 9.

Boundary conditions are prescribed following the approach of Carlson.[51] The boundary condition at the entrance of the wind tunnel is a pressure inlet, where the total pressure and total temperature are prescribed. The outlet boundary condition corresponds to the pressure outlet, where the static pressure is specified. The total conditions are determined from the ambient conditions, which are p_o = 101964 Pa and T_o = 294.3 K. The measured velocity in the test section without the airfoil installed (u = 15 m/s) is used to calculate the outlet static pressure. The static pressure in the test section is approximated using one-dimensional compressible flow theory, which is p_{test} = 101, 828.7 Pa.

The Mach number and static temperature in the test section as predicted by CFD is $M_{\text{test}} = 0.0436$, and T_{test} = 294.15 K. Static pressure at the exit of the tunnel is calculated by the area ratio, which is $A_t/A_e = 0.266$. Through this relation, we find $M_{\text{exit}} = 0.012$. Finally, the static pressure at the exit of diffuser is p_{exit} = 101, 955 Pa.

CFD - Modeling plasma actuators

Actuators within the CFD simulation are located at the exact same positions and in the same shapes as the fan and serpentine actuators in the wind tunnel. Forcing functions are applied in FLUENT through the user defined function module. These are calibrated through comparisons with the actuators mounted in the wind tunnel with the tunnel off. In the simulation, the body force induced by the actuators is modeled using a simplified distribution proposed by Singh and Roy.[52] The magnitude of the force is obtained empirically with experimental data from the wind tunnel measurement with the tunnel off. The forces from the actuators are

Table 3. Parameters of the CFD forcing functions for plasma actuation.

F_{xo}	F_{yo}	β_x	β_y	y_b	T
2.6	2.0	8×10^5	10^7	0.00333	1500

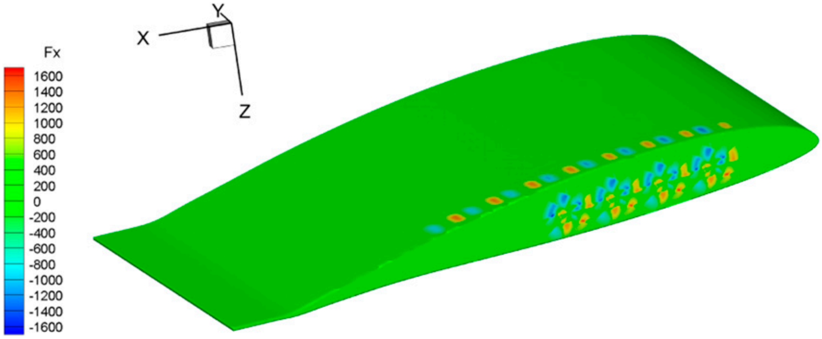

Figure 10. Body force, F_x, on the airfoil. Unit N/m^3.

$$F_x = T\frac{F_{xo}}{\sqrt{F^2_{x,0}+F^2_{y,o}}} \times \exp\left[-\left(\frac{(x-x_o)-(y-y_o)}{y-y_o+y_b}\right)^2-\beta_x(y-y_o)^2\right] \tag{3}$$

and

$$F_y = T\frac{F_{yo}}{\sqrt{F^2_{x,o}+F^2_{y,o}}} \times \exp\left[-\left(\frac{(x-x_o)}{y-y_o+y_b}\right)^2-\beta_y(y-y_o)^2\right] \tag{4}$$

where T is a scaling coefficient that modulates the simulated strength of the actuator, $F_{x,o}$ and $F_{y,o}$ are average thrust parameters obtained by solving the air-plasma equations, and β_x, β_y, and y_b are functions of the dielectric material and actuator design that control the spatial extent of the exponential function. Lastly, x_0 and y_0 describe the location of the actuator where x_o is the midpoint between the electrodes and y_o is at the dielectric surface. For this work, T corresponds to a value that induces a peak velocity magnitude between 4 m/s and 5 m/s in a quiescent simulation to match the strength of a physical plasma actuator,[53] and reference values from the literature are used for $F_{x,o}$, $F_{y,o}$, β_x, β_y, and y_b.[52] Parameters of the CFD plasma actuators are shown in Table 3.

CFD - Plasma actuators

The plasma actuators on the HH-02 airfoil consist of a single serpentine and a series of fans. We position the serpentine actuators starting at 1.58 inches from the leading edge with a spacing of 20 mm and width of 4 mm. This geometry is mapped onto the surface of the computational surface grid of the airfoil. The geometry points are then read by the solver to calculate the body force induced by the actuator in each element. Fan actuators are placed on the wingtip surface. Each fan actuator has five blades with three arcs each. Contours of the forcing functions on the HH-02 airfoil defined by equations (3) and (4) are shown in Figures 10–12.

Blade vortex interaction noise modeling

We now describe the BVI noise prediction model and its implementation. Our model is based on a slightly modified form of the Fundamental Rotorcraft Acoustic Modeling from Experiments (FRAME) technique developed by Greenwood et al.[43,44] The BVI noise is calculated by coupling a wake-vortex model with the Ffowcs Williams and Hawkings[48] (FWH) solver. The wake-vortex model predicts the alteration of pressures on the blades during descent, which corresponds to maximum BVI noise cases. The wake-vortex model consists of various semi-empirical relations predicting the path and the strength of the tip vortex. The FWH solver is then used to predict radiated BVI noise at the observer location using the induced velocity and pressure on the rotor blades. Using a wake-vortex model in conjunction with the FWH solver significantly reduces the computational expense when compared to predicting the BVI noise from a time-resolved numerical simulation. However, the wake-vortex model consists of several calibration coefficients. These coefficients are calibrated using the full-scale measurements of the UH-1H helicopter by Boxwell and Schmitz.[45] We use the same model with the calibrated coefficients to predict the reduction of BVI noise due to plasma actuation for the HH-02 airfoil. We note that dielectric barrier plasma actuators operate at kHz frequencies producing electrically induced, non-aerodynamic, broadband self-noise.[39,54] While including this might improve predictions, the self-noise was at a low level and plasma induced noise is not included to reduce computational complexity.

Wake-vortex model

A wake-vortex model is implemented based on the work of Landgrebe[55] and Beddoes.[56] The wake-vortex model is used to calculate the loading perturbations due to the tip vortices on the rotor blades. The position of the wake-vortex and its strength is based on the combined freestream flow and prescribed inflow distribution over the rotor. The path of the tip vortex location is ascertained using the same equations mentioned by Greenwood et al.[43,44] Various empirical coefficients are involved in predicting the path of the tip vortex. These coefficients are calibrated using the experimental measurements. The vortex core size and its growth rate are calculated using

$$\bar{r}_c = \left(\bar{r}_\circ^2 + 4C_v\varphi\right)^{1/2} \tag{5}$$

where $\bar{r}_\circ$ is the initial vortex core size, $\bar{r}_c$ is the vortex core size at a wake age, ϕ, and C_v is the vortex core growth coefficient. The strength of the tip vortex directly influences the blade vortex interaction and is given as

$$\bar{\gamma}_v(\psi_v) = \bar{\Gamma}(\gamma_\circ + \gamma_{1\,s}\sin\psi_v + \gamma_{1c}\cos\psi_v) \tag{6}$$

where the nominal vortex strength $\bar{\Gamma}$ is determined from the ideal vortex strength Γ as

$$\bar{\Gamma} = \frac{\Gamma}{\Omega R^2} = \frac{2\pi c_T}{b} \tag{7}$$

Here, $\gamma_\circ$, γ_{1c}, and γ_{1s} are the mean, longitudinal, and lateral vortex strength coefficients, respectively. These coefficients are calibrated empirically along with the coefficients involved in predicting the path of the vortex. The coefficient of thrust is represented by c_T. The number of blades, radius of the rotor, and the angular rotational speed of the rotor are denoted by b, R, and Ω, respectively.

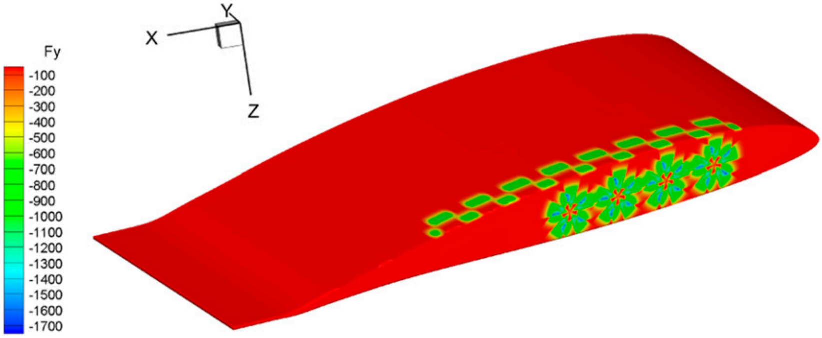

Figure 11. Body force, F_y, on the airfoil. Unit N/m^3.

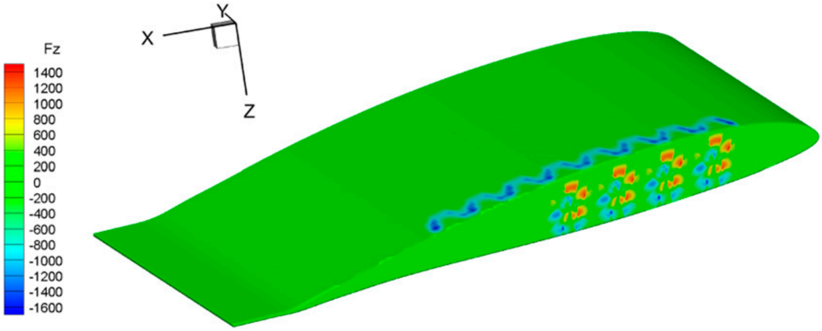

Figure 12. Body force, F_z, on the airfoil. Unit N/m^3.

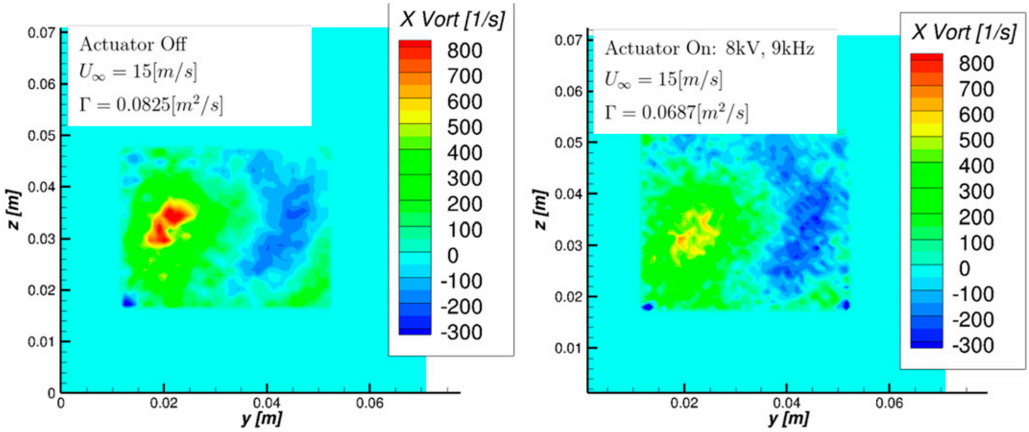

Figure 13. Plot of the *Q*-criterion as a function space for a freestream speed of 15 m/s obtained via particle image velocimetry. Note the reduction in Γ for the actuator on case (right).

The Biot–Savart law[47] is used to find the induced velocity on the rotor from the tip wake-vortex. The non-dimensional swirl velocity is calculated using the Vatistas et al.[57] model as

$$\frac{v_\theta}{\Omega R} = \frac{\overline{\gamma}_v \overline{r}}{2\pi\left(\overline{r}_c^4 + \overline{r}^4\right)^{(1/2)}} \tag{8}$$

The velocity perturbations on the rotor cause unsteady aerodynamic loading effects on the rotor blade. The unsteady aerodynamic loading effects are accounted for by using a two-dimensional incompressible indicial aerodynamics method by Greenwood et al.[43,44] A simplified approach using Bernoulli's equation is implemented in the current work.

Ffowcs Williams and Hawkings solver

The FWH solver is extensively used to predict the helicopter or rotor noise.[58] Three different source terms, viz. the thickness, loading, and quadrupole terms are present on the right-hand side of the

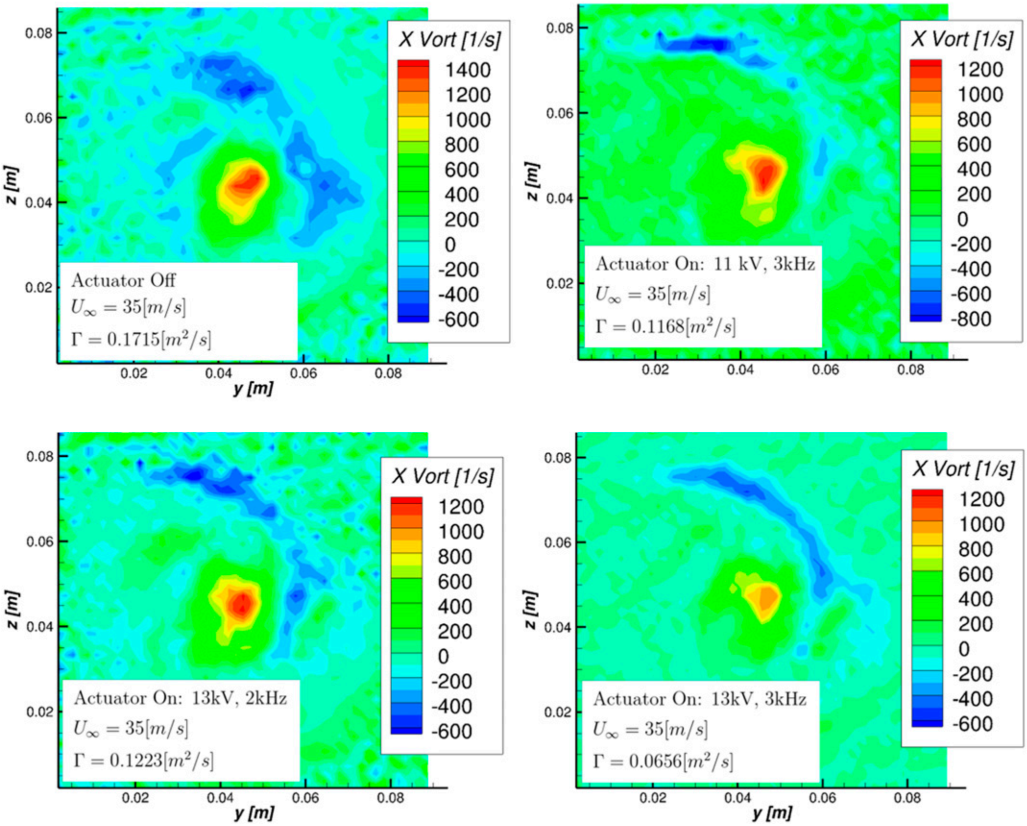

Figure 14. Plot of the vorticity as a function space for a freestream speed of 35 *m/s* obtained via particle image velocimetry. Note the lower circulation, gamma, for the three actuator on cases in comparison to the actuator off cases.

FWH equation. As BVI is generated due to the pressure alteration on the rotor blade, the pressure loading term in the FWH equation is most important for BVI prediction. We choose the FWH surface such that it coincides with the rotor surface. Farassat analytically derived the thickness and loading noise terms of the FWH equation in his Formulation I and IA using the free-space Green's function. He obtained the analytical loading noise in Formulation IA as

$$4\pi p_L'(\mathbf{x},t) = \int_f \left[\frac{\dot{p}\cos\theta}{cr(1-M_r)^2} + \frac{\hat{r}_i \dot{M}_i p\cos\theta}{cr(1-M_r)^3}\right]_{ret} \\ + \left[\frac{p(\cos\theta - M_i n_i)}{r^2(1-M_r)^2} + \frac{(M_r - M^2)p\cos\theta}{r^2(1-M_r)^3}\right]_{ret} dS \tag{9}$$

Here, $\boldsymbol{r}$ represents the distance between the observer location, $\boldsymbol{x}$, and the source location, $\boldsymbol{y}$. The FWH surface is defined by f, and the surface area of the FWH surface is denoted by S. The Mach number of the FWH surface is denoted by $\boldsymbol{M}$. The ambient speed of sound is represented by c and the gage pressure on the FWH surface is represented by p. The subscript r denotes the component of the

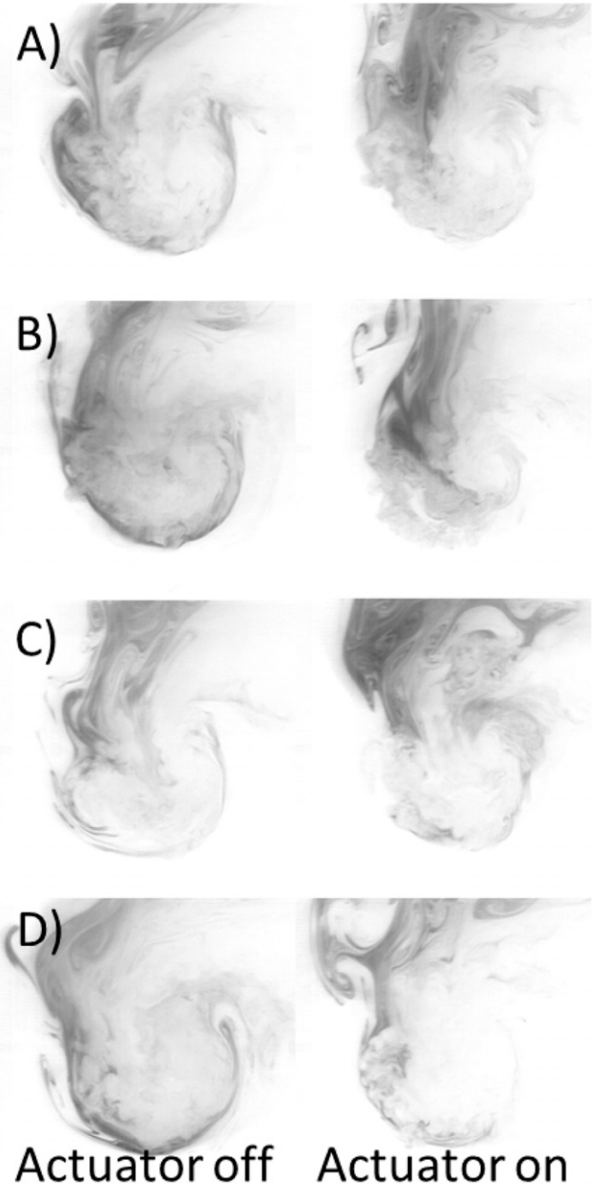

Figure 15. Short exposures of smoke visualization with the actuator off (left) and actuator on (right).

field-variable in the radial direction from the source to the observer. A dot above a field-variable denotes the time derivative.

All the terms inside the integral equation (9) are evaluated at retarded time. The face areas, face centers, and face normals are calculated at each time-step based on the cell-connectivity and motion of the FWH surface. A source-time dominant algorithm proposed by Brentner and Farassat[58] is used in the present work to evaluate equation (9). Using this approach, the time when the acoustic signal

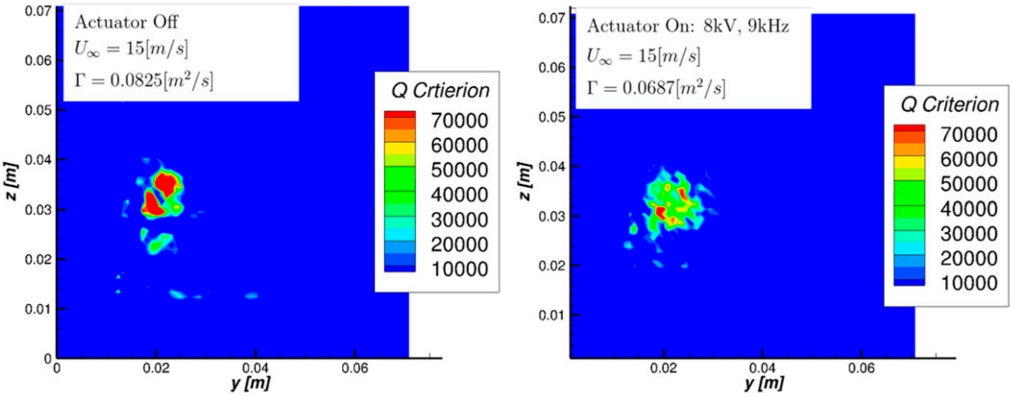

Figure 16. Contours of the Q-criterion as a function space for a freestream speed of 15 m/s obtained via particle image velocimetry.

reaches the observer location is calculated using $t = \tau + rc_0^{-1}$, where t is the observer time and τ is the source time. The acoustic signal from each face on the FWH surface contributes to the final acoustic pressure fluctuations at a given time for the observer location. Interpolation is performed in order to obtain the final acoustic pressure at the observer location at a given time.

The operating conditions and the rotor geometry are used as inputs to the BVI model. The location and radius of the wake-vortex is determined using empirical relations dependent on advance ratio, μ, inflow ratio, λ, advancing tip Mach number, M_{AT}, and coefficient of thrust, C_T. The strength of the vortex, Γ, is determined from the experimental measurements. Note that there is uncertainty associated with predicting the location and radius of the vortex. Calibration using various experimental databases is required for an accurate prediction. The aerodynamic loading pressure on the rotor blades are obtained from CFD simulations.

The loading pressure effects, consisting of aerodynamic loading and pressure loading due to BVI, and the motion of the rotors are used as an input to the FWH solver to obtain the noise at the observer location. The loading pressure due to plasma actuators are relatively small compared to the overall aerodynamic loading. Therefore, the plasma actuators themselves have little direct effect on BVI noise. Hence, the model is relatively insensitive to the low amplitude loading pressure when compared to the high-amplitude pressure due to BVI.

Results

Experimental results

We tested the actuator on and actuator off at both 15 m/s and 35 m/s. We use the circulation at 0.4c from the trailing edge to quantify the effectiveness of the actuator in reducing vortex strength. For each flow speed, we employed different voltage and frequency values to identify the most effective control on the tip vortex for the parameter set used. We find that the circulation for both 15 m/s and 35 m/s tip speeds at 0.4c from the trailing edge is lower for the actuator “on” case (Figures 13 and 14). The circulation was reduced by 17% and 62% for the 15 m/s and 35 m/s tip speed cases, respectively.

Based on the visualizations, we find that the outer edges of the vortex continually break down and form again. From a qualitative perspective, it appears that actuators encourages the breakdown of these edges and discourages the formation of the edges (Figure 15). The breakdown of the vortex

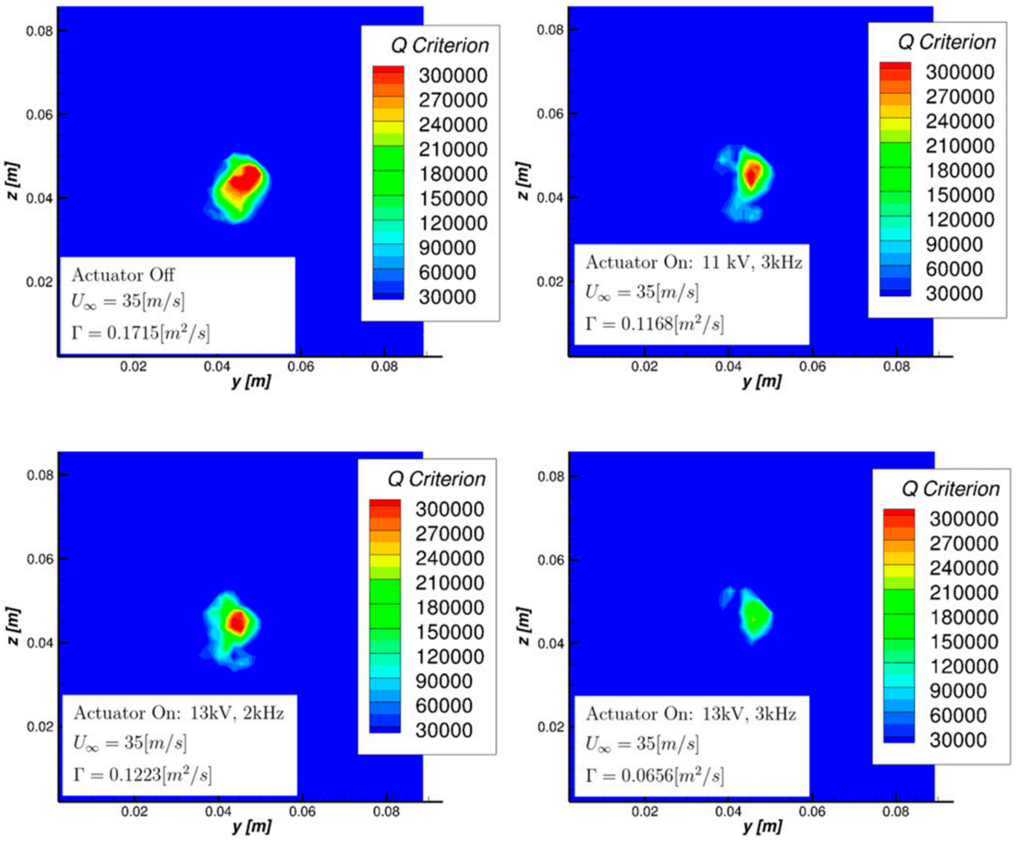

Figure 17. Contours of the Q-criterion as a function space for a freestream speed of 35 m/s obtained via particle image velocimetry.

edges appears to disrupt vortex formation and slow down the core of the vortex. Due to the placement of the actuator, forcing is applied at the inception of the wing tip vortex. The actuator induces small oscillations into the outer edge of the vortex as it forms. We observe that the outer edge grows and becomes unstable as the vortex travels downstream of the airfoil. The unstable outer edge of the vortex mixes high vorticity core fluid with low vorticity freestream fluid, therefore reducing the strength of the core. We examine the Q criterion to visualize the vortex. The Q-criterion of both the 15 m/s and 35 m/s cases are shown in Figures 16 and 17.

Note that we did not perform a study optimizing the placement of the actuator on the airfoil; therefore, it may be possible to further reduce circulation due to wing tip vortex for specific airfoils.

Computational fluid dynamics results

We now present results from our numerical study. We first examine the changes in the Q-criterion, which is presented in Figure 18. Here, the iso-surface of Q-criterion at $Q = 1000$ is colored by streamwise velocity. The wing tip vortex rolls up from the pressure side to the suction side and has an irregular shape. This illustrates that the nature of the tip vortex is captured by the steady RANS simulation. Figure 19 presents the streamwise velocity on the $z = 0$ slice. We find that the maximum

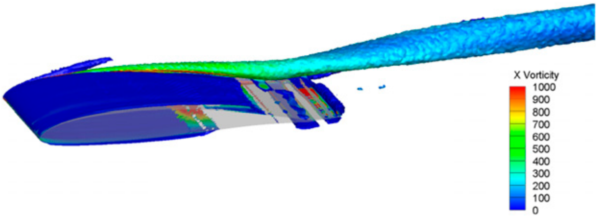

Figure 18. $Q = 1000$ iso-surface colored by streamwise vorticity [1/s].

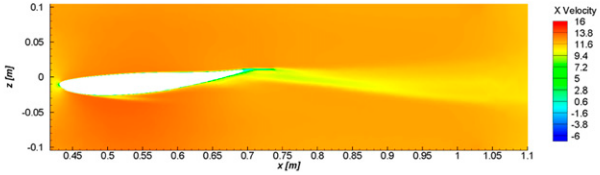

Figure 19. Streamwise velocity at $y = 0$ [m/s].

streamwise velocity in the test section is approximately 15.3 m/s, which is close to the desired freestream velocity.

The x-vorticity contour for both actuator “off” and “on” cases for 15 m/s tip velocity at $x/c = 0.1$ are presented in Figure 20(a) and (b), respectively. The circulation is calculated using equation (1), and corresponds to 0.3116 m^2/s and 0.297 m^2/s for the actuator “off” and “on” cases, respectively. Also, the x-vorticity at $x/c = 0.4$ for the actuator “off” and “on” cases for 15 m/s tip velocity are shown in Figure 21(a) and (b), respectively. The circulation for both simulations decreases due to dissipation, which are 0.3080 m^2/s and 0.2943 m^2/s, respectively. Numerically, we find that the plasma actuation on the airfoil can reduce the circulation of the tip vortex by approximately 4.7%.

Validation of the BVI noise model

We validate the prediction results from our BVI noise model with the experimental measurements of Boxwell and Schmitz.[45] Boxwell and Schmitz[45] use a full-scale two-blade UH-1H rotor with a $-10.9°$ linearly twisted NACA0012 airfoil and an aspect ratio of 13.713. The radius of the rotor is 24 ft, and the chord of the blade is 1.75 ft. The observer is located below the rotor plane at an angle of 30° and is located at a distance of 75 ft from the main rotor. We use the same airfoil characteristics as Boxwell and Schmitz[45] for our validation case, without blade twist as is appropriate in the non-rotating simulation.

The path of the tip wake-vortex is computed using the equations mentioned by Greenwood et al.[43,44] and are plotted in Figure 22. The vortices that are shed from two blades are shown in different colors in Figure 22 for a vehicle moving forward in the x direction. The induced velocity on the rotor plane is calculated using equation (8) and is shown in Figure 23. Different localized regions on the rotor plane that are affected by the tip wake-vortices are observed. The BVI noise is generated when the rotor blades pass through these localized regions. The locations of the wake-vortex and the induced velocity results look qualitatively similar to the results of Greenwood et al.[43] We obtain the loading pressure from the induced wake-vortex at every location of the rotor using Bernoulli’s equation. Finally, we use the loading pressure induced by the wake-vortex in the FWH solver to calculate BVI noise.

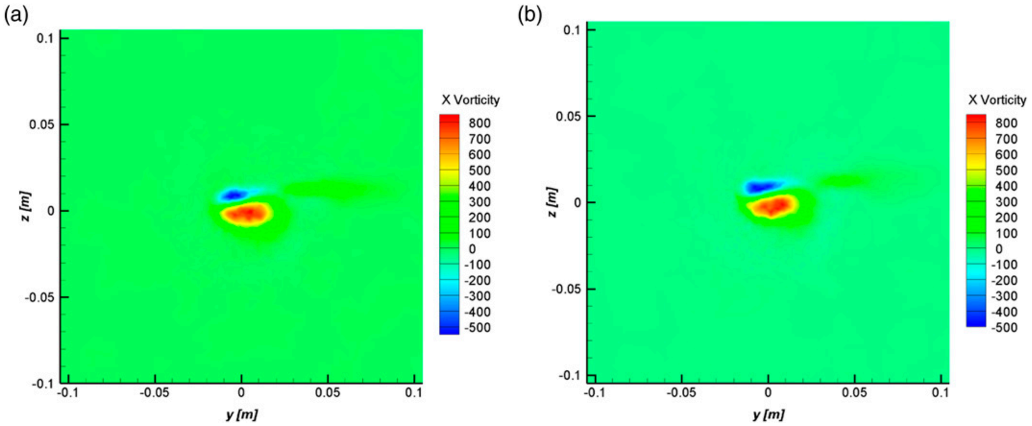

Figure 20. Axial vorticity at $x/c = 0.1$ [1/s]. (a) Actuator off and (b) Actuator on.

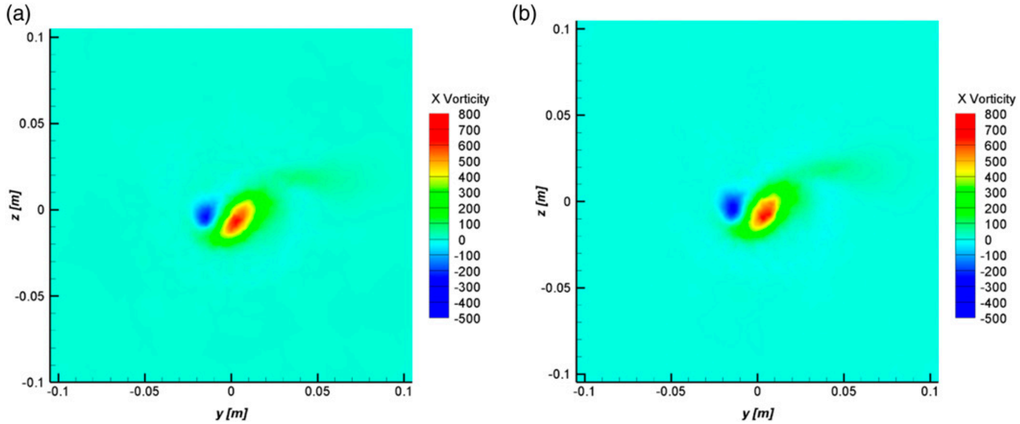

Figure 21. Axial vorticity at $x/c = 0.4$ [1/s]. (a) Actuator off and (b) Actuator on.

The coefficient of pressure values at different Mach and Reynolds numbers for the NACA 0012 airfoil section have been obtained by Ladson.[59] We use the coefficient of pressure measurements by Ladson[59] to obtain the pressure loading on the rotor surfaces. The loading due to the tip vortex is calculated additionally using the wake-vortex model and is added to the aerodynamic loading values. We use the combined pressure loading on the rotor surfaces as an input to the FWH solver to calculate the acoustic pressure at the observer location.

We now calibrate our acoustic model using the full-scale measurements from the UH-1H helicopter. The operating conditions for the UH-1H helicopter are $M_{AT} = 0.869$, $v_T = 87$ knots, $\mu = 0.181$, and $c_T = 0.00301$, where M_{AT} is the advancing tip Mach number, v_T represents the true airspeed of the vehicle, μ is the advance ratio of the vehicle, and c_T represents the coefficient of thrust. We use the same experimental conditions for calibrating various coefficients in the wake-vortex model. The calibrated coefficients related to the strength of the vortex in equation (6) are $\gamma_\circ = 3.501$, $\gamma_{1s} = -6.366$, and $\gamma_{1c} = 6.366$. Note that all the calibrating coefficients are calibrated using one operating condition of the full-scale helicopter and have not been optimized for a range of

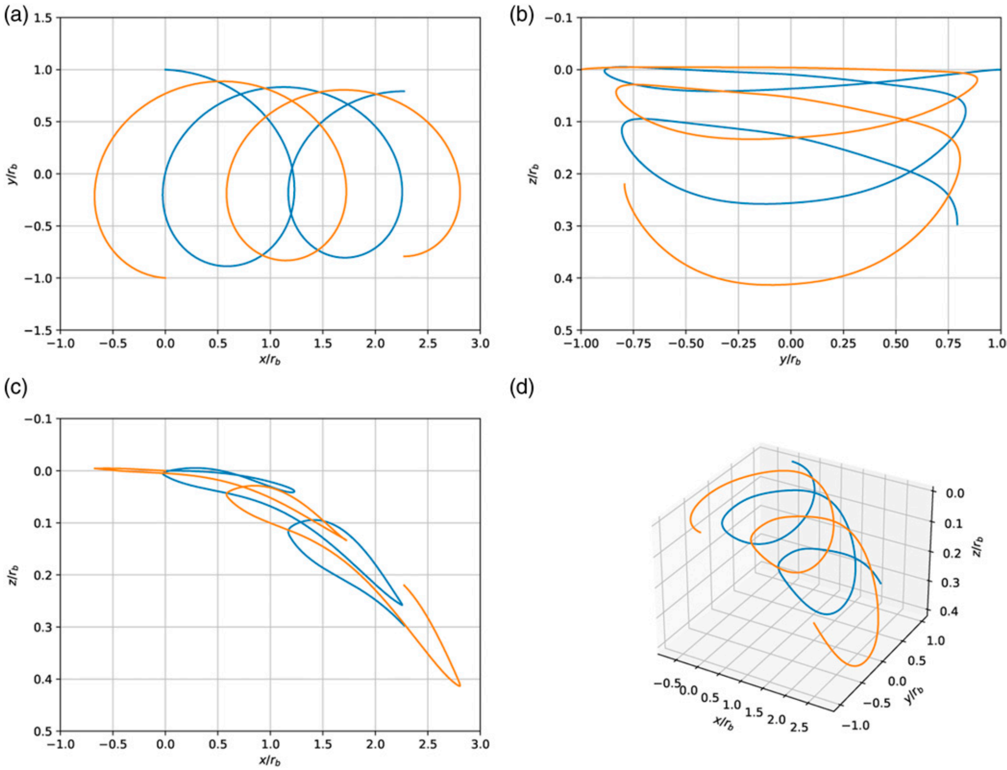

Figure 22. Different locations of the trailing tip vortices. The orange and blue lines denote the location of the tip vortices from two different blades. The plots are non-dimensionalized with the rotor radius. The blades of the rotor are centered at the origin. (a) \$x - y\$ position of the tip vortex, (b) \$y - z\$ position of the tip vortex, (c) \$x - z\$ position of the tip vortex, and (d) Three dimensional position of the tip vortex.

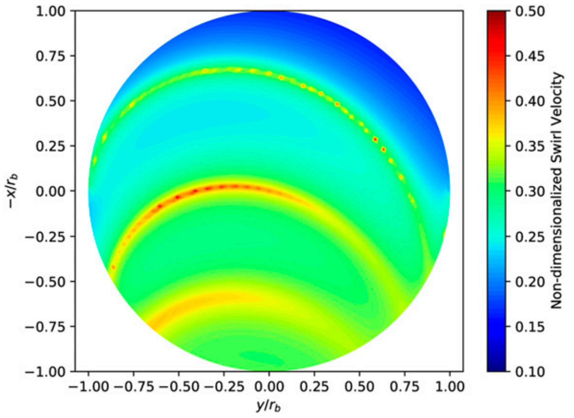

Figure 23. Non-dimensionalized swirl velocity on the rotor surface.

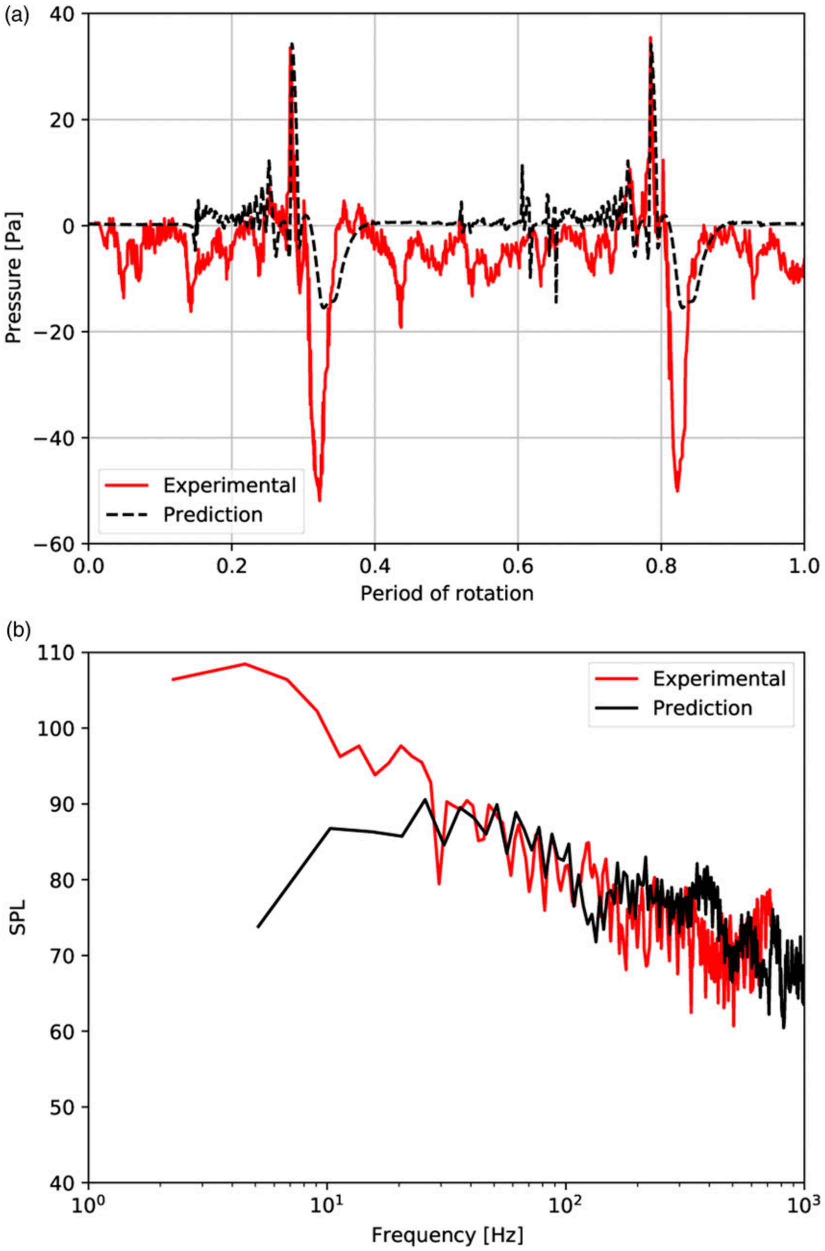

Figure 24. Blade vortex interaction noise for UH-1H helicopter. (a) Comparison of the time-domain acoustic results for one blade revolution. Note the positive portion of the waveform corresponds to BVI noise and the large negative peaks correspond to thickness noise; (b) Comparison of the acoustic spectra.

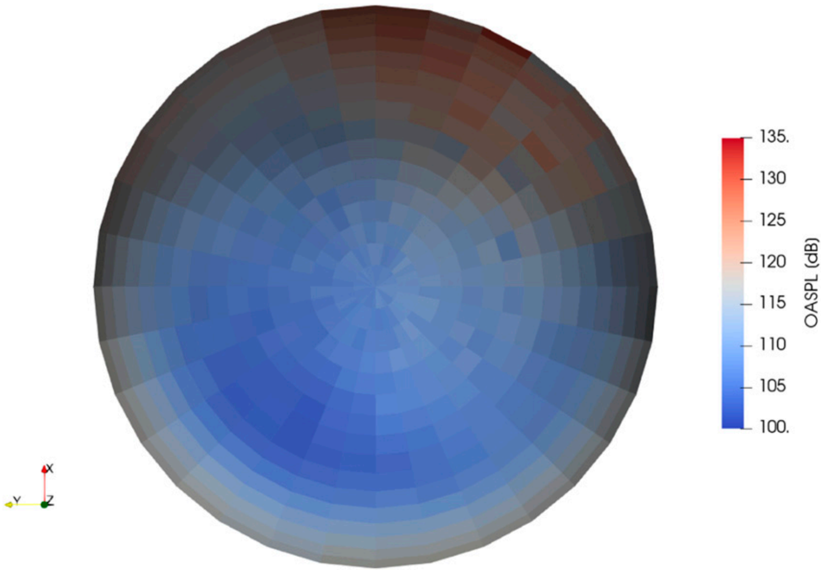

Figure 25. Predicted directivity of the BVI noise for the UH-1H helicopter operating at M_{AT} = 0.869.

Table 4. OASPL and strength of vortex for the 15 m/s case.

	Γ (m^2/s)	OASPL (dB)
Actuator off	0.08253	45.56
Actuator on	0.06867	42.50
Γ◦ Ratio	0.8320	
OASPL reduction		−3.060

operating conditions. Greenwood et al.[43,44] calibrated the coefficients in their BVI model using an optimization technique at multiple observer locations and operating conditions using an extensive experimental database. However, in our current work, we are mainly interested in the reduction of noise due to plasma actuators. Hence, there will be some uncertainties present in the prediction of absolute OASPL due to calibration of the coefficients at a single operating condition. However, since the BVI pressure directly depends on the vortex strength, Γ, the reduction of vortex strength by a given factor should give us an accurate value of the reduction of BVI noise.

The growth rate of the vortex c_v is calibrated using the work of Moore and Saffman.[46] The radius of the vortex where the tangential velocity is maximum is given by Moore and Saffman[46] as

$$r = 2.92\left(\frac{vd}{U}\right)^{\frac{1}{2}} \tag{10}$$

where v is the kinematic viscosity, d is the distance traveled by the vortex downstream of the wing, and U is the freestream velocity in fixed-wing coordinates. We compare equation (10) with equation (5) to obtain the growth rate of the vortex, c_v.

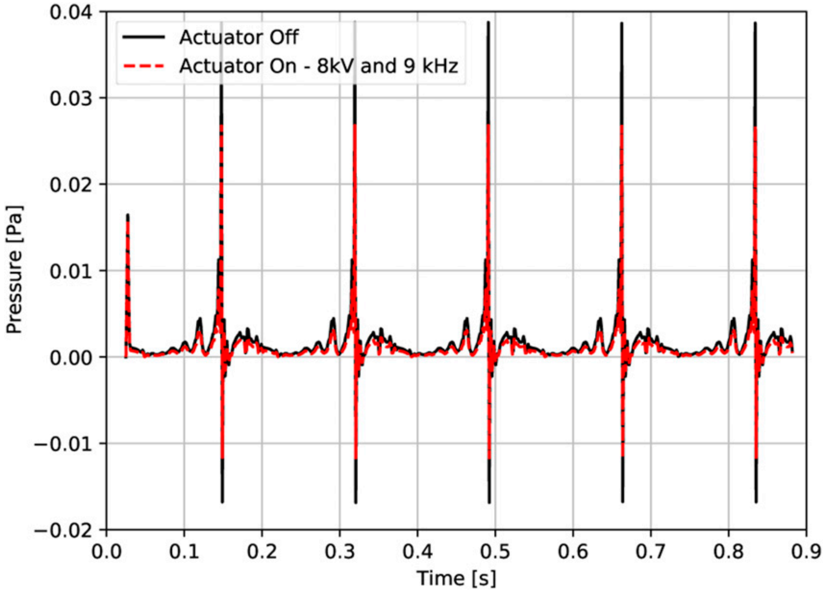

Figure 26. Prediction of the acoustic signal for 15 m/s case with plasma actuators on and off.

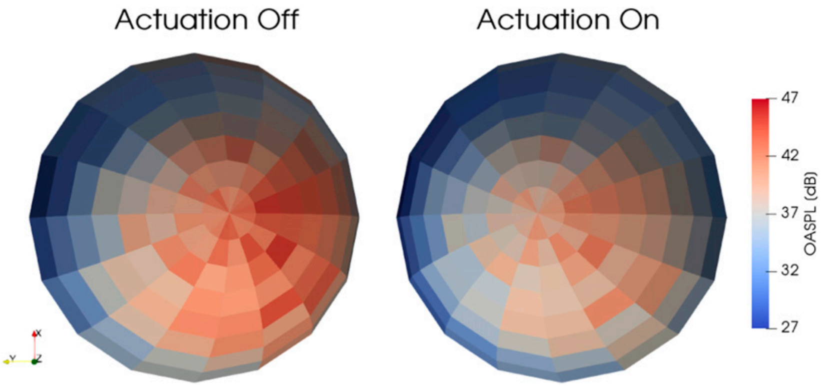

Figure 27. Comparison of the directivity contours of BVI on a hemisphere with plasma actuation on and off for 15 m/s case.

Table 5. OASPL and strength of vortex for 35 m/s case.

	Γ (m^2/s)	OASPL (dB)	Γ ratio	OASPL reduction
Actuator off	0.1715	60.41	—	—
11 kV, 3 kHz	0.1168	53.95	0.6811	–6.460
13 kV, 2 kHz	0.1223	54.70	0.7131	–5.710
13 kV, 3 kHz	0.06558	45.89	0.3824	–14.52

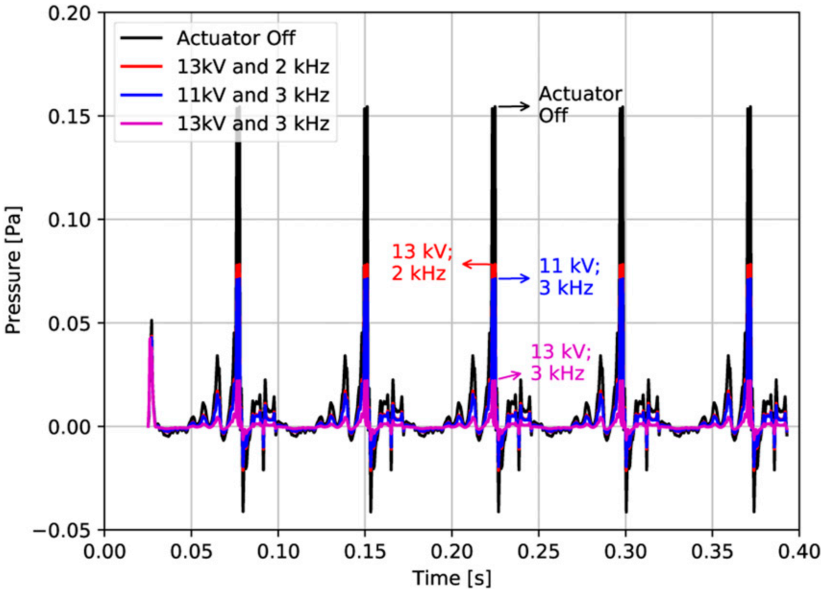

Figure 28. Prediction of the acoustic signal for 35 m/s case with plasma actuators on and off.

A comparison of the time-domain acoustic pressure and the pressure spectrum of the predicted results using the model with the full-scale measurements is shown in Figure 24. Note that the full-scale measurements of the UH-1H helicopter consist of all the noise sources including the thickness noise, engine noise, tail-rotor noise, etc. In the present work, we are interested in predicting the BVI noise only.

Very good agreement is found in the prediction of the magnitude as well as the period of the BVI noise peak in Figure 24(a). The magnitude of the BVI peak is predicted within an error of 1 Pa. However, the negative thickness noise peak is not predicted well with the FWH solver. The same discrepancy with the thickness noise with the FWH acoustic analogy and the experiments were observed by Schmitz and Yu.[60] The pressure spectrum also compares well with the experimental spectrum in Figure 24(b). The high-amplitude low-frequency discrepancy can be attributed to the thickness noise, which is not accounted for by the FWH solver.[60] A directivity plot using the same operating conditions over a hemisphere below the helicopter is shown in Figure 25. A hemisphere of 75 ft. is constructed below the rotors and in the direction of the helicopter. The hemisphere is moving in the vertical direction along $+x$ direction. The acoustic model is run at different locations on the hemisphere. The BVI noise is dominant along the direction of travel of the helicopter.

Predictions of altered BVI noise via plasma actuation

We now use the same calibration coefficients for the prediction of BVI noise with and without plasma actuation. A combination of experimental and CFD results are used as an input to the acoustic model. The HH-02 airfoil is used for the prediction. The design of the airfoil and the operating conditions are kept the same as the wind-tunnel experiments. The aspect ratio of the airfoil is six. Five blades are selected to maximize the number of blade-vortex interactions in one rotation.

Predictions of three different cases with varying tip velocities at 15 m/s, 35 m/s, and 150 m/s are performed. The pressure coefficients are obtained from the CFD simulations. The strength of the

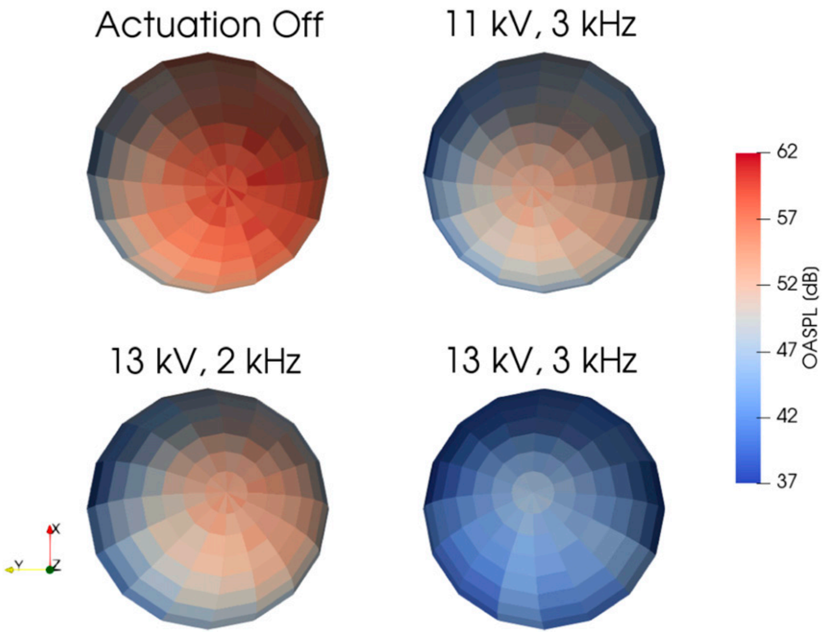

Figure 29. Comparison of the directivity contours of BVI on a hemisphere with plasma actuation on and off for 35 m/s case.

Table 6. OASPL and strength of vortex for 150 m/s case.

	OASPL (dB)	OASPL reduction (dB)
Baseline	99.25	–
$0.9\Gamma_\circ$	97.42	1.83
$0.8\Gamma_\circ$	95.37	3.88
$0.7\Gamma_\circ$	93.05	6.20
$0.6\Gamma_\circ$	90.37	8.88

vortex and the radius of the vortex are obtained from the PIV measurements from the experiment. We use the strength of the vortex, Γ as an input to the acoustic model. The coefficient of thrust is calculated from the operating conditions and the strength of the vortex using equation (7). We quantify the noise reduction using a ratio of the strength of the vortex when plasma actuation is “on” to the strength of the vortex when the plasma actuation is “off.” We multiply this ratio with equation (6) to obtain the reduced strength of vortex as

$$\overline{\gamma}_v(\psi_v) = \frac{\Gamma_{\text{on}}}{\Gamma_{\text{off}}}\overline{\Gamma}(\gamma_\circ + \gamma_{1\,s}\sin\psi_v + \gamma_{1c}\cos\psi_v) \tag{11}$$

The change in the radius of the vortex does not make a significant difference in the final BVI noise. Hence, the noise reduction due to the reduction in the strength of the vortex is analyzed.

The strength of the vortex and the corresponding OASPL obtained from the acoustic model for the 15 m/s case is tabulated in Table 4. The prediction of time-domain acoustic signal for a tip

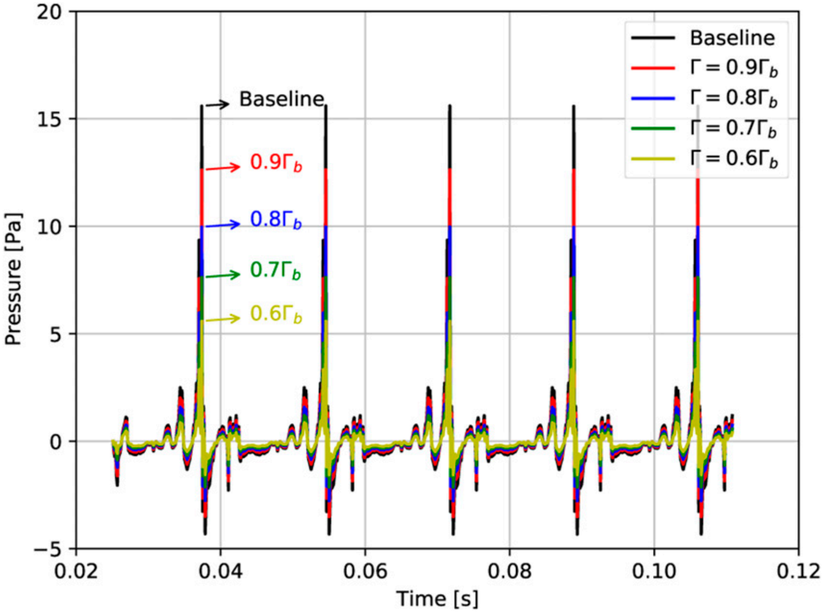

Figure 30. Parametric study of the acoustic signal for 150 m/s case with different vortex strengths.

velocity of 15 m/s is shown in Figure 26. The observer is located at a distance of 9 m from the center of the rotor. The strength of the vortex is reduced by a ratio of 0.832 when the plasma actuator is turned on. The plasma actuator operates at a voltage of 8 kV and fluctuates with a frequency of 9 kHz. The acoustic pressure reduces from 0.039 Pa to 0.027 Pa when the plasma actuator is switched on. Correspondingly, the OASPL reduces by 3.06 dB when the plasma actuator is turned on. The directivity of the BVI noise at different locations on the hemisphere is shown in Figure 27. The radius of the hemisphere is 9 m and is aligned similarly to the validation case. A constant reduction of 2 to 3 dB is observed at every location in the hemisphere.

The operating conditions, that is, the voltage and the frequency of the plasma actuator is varied for the 35 m/s case. Measurements of the strength of the vortex for three different combinations of the operating conditions of the plasma actuator are obtained. The results of the strength of the vortex and the OASPL reduction from the acoustic model for the 35 m/s case are tabulated in Table 5. The comparison of the time-domain acoustic signal for the different cases is shown in Figure 28. A maximum reduction in the strength of the vortex is obtained using a 13 kV and 3 kHz plasma actuator. The strength of the vortex reduces by 61.76%. The acoustic pressure reduces from 0.155 Pa to 0.02 Pa. Correspondingly, a 14.52 dB reduction is obtained. The directivity contours on the hemisphere are shown in Figure 29. The noise reduction of 5 to 6 dB for the 11 kV at 3 kHz and 13 kV at 2 kHz actuators are almost equal at every location.

We directly reduce the strength of noise by reducing the strength of the vortex using plasma actuators. Hence, an almost equal reduction is observed at every location on the hemisphere in Figures 27 and 29 when the plasma actuator is turned on.

A parametric study is performed for the high-speed 150 m/s case. A vortex strength, $\Gamma = 0.772\ \mathrm{m^2/s}$ corresponding to a thrust coefficient of $c_T = 0.002$ is used for the parametric study. We observe the reduction of OASPL of the BVI noise by varying the strength of the vortex. The strength of the vortex is reduced in increments of 10% from the baseline vortex strength. The results of the OASPL reduction are tabulated in Table 6. The time-domain acoustic pressure for various strengths of the tip vortex is shown in Figure 30. The acoustic pressure reduces from 15.5 Pa to 5.8 Pa when the strength of the vortex is reduced by 40%. Correspondingly, a reduction of 8.88 dB in the OASPL is observed.

Summary and conclusions

We performed a fundamental investigation to ascertain if plasma actuation of rotor tip vortices can reduce their strength. Through CFD and acoustic modeling the reduction of vortex strength is predicted to lead to reduced noise. We confirmed with PIV that plasma actuators are able to reduce the strength of tip vortices within stationary frame wind tunnel tests. The PIV results indicate the plasma actuators reduce Γ by more than 60% relative to the non-actuated flow, for the higher speed case. These tests along with CFD supported a conclusion of significant reduction of BVI noise through a slightly modified BVI noise prediction method. With both quantitative and qualitative results showing the same trends, we conclude that plasma actuators have a high probability of reducing strength of tip vortices and BVI noise. The actuators for these experiments expended approximately 6–7 W, which is orders of magnitude lower than the power transmitted by rotors at this scale. This low power requirement with quantitative estimates of BVI noise reduction supports higher fidelity experiments for practical UAM and DEP systems. We recognize that the uncertainty regarding the absolute OASPL values is fairly high; however, we maintain that the differential estimates with and without actuation should be sufficiently accurate for purposes of evaluating viability of the concept.

In the future, we plan to perform similar experiments in a rotating framework within an anechoic wind tunnel to measure the actuator-induced changes in sound intensity and directivity. Results of these new experiments, based on the present fundamental study, will enable direct assessment of the acoustic model accuracy. In addition, optimization of actuator position and electrical parameters at the higher relative wind speeds experienced in DEP rotors will be undertaken.

Acknowledgements

The authors acknowledge the support of this work by NASA STTR Contract 80NSSC19C0540 with Surf-Plasma and the University of Florida.

Declaration of conflicting interests

The author(s) declared no potential conflicts of interest with respect to the research, authorship, and/or publication of this article.

Funding

The author(s) disclosed receipt of the following financial support for the research, authorship, and/or publication of this article: This study was supported by National Aeronautics and Space Administration; 80NSSC19C0540.

ORCID iDs

Trushant K Patel https://orcid.org/0000-0001-7187-0642
Steven AE Miller https://orcid.org/0000-0002-3697-3037

References

1. Schlinker RH and Amiet RK. Rotor-vortex interaction noise. In 8th Aeroacoustics Conference. AIAA Paper No. 83-0720. 11-13 April 1983, Atlanta, GA. DOI:10.2514/6.1983-720.
2. Wang CC and Roy S. Microscale plasma actuators for improved thrust density. *J Appl Phys* 2009; 106(1): 013310. DOI: 10.1063/1.3160304.
3. Roy S and Wang CC. Bulk flow modification with horseshoe and serpentine plasma actuators. *J Phys D Appl Phys* 2008; 42(3): 032004. DOI: 10.1088/0022-3727/42/3/032004.
4. Singh KP and Roy S. Modeling plasma actuators with air chemistry for effective flow control. *J Appl Phys* 2007; 101(12): 123308. DOI: 10.1063/1.2749467.
5. Wang CC, Durscher R and Roy S. Three-dimensional effects of curved plasma actuators in quiescent air. *J Appl Phys* 2011; 109(8): 083305. DOI: 10.1063/1.3580332.
6. Krantz DS and Lazar JD. The stress concept: issues and measurement. In: Julius S and Bassett DR (eds). *Handbook of Hypertension. Vol.9: Behavioral Factors in Hypertension*. Amsterdam. Elsevier Science Publishers, 1987, Vol. 9, pp. 43–58.
7. Parenko NM and Wjshtpan WF. About the influence of the human organism of noise and local vibrations not surpassing the maximum allowable intensities (In Russian). *Gig i Sanit* 1967; 32: 25–26.
8. Cohen S and Weinstein N. Nonauditory effects of noise on behavior and health. *J Soc Issues* 1981; 37(1): 36–70. DOI: 10.1111/j.1540-4560.1981.tb01057.x.
9. Passchier-Vermeer W. Noise and health of children. Technical Report PG/VGZ/2000.042. Leiden, Netherlands: TNO Prevention and Health, 2000.
10. Bullen RB. The effects of aircraft noise: current knowledge and future research directions. *Bull Aust Acoust Soc* 1984; 12: 75–79.
11. Meecham WC and Smith HG. Effects of jet aircraft noise on mental hospital admissions. *Br J Audiol* 1977; 11(3): 81–85. DOI: 10.3109/03005367709078838.
12. Portugal Atencio SE. *Design and improvement of dielectric barrier discharge (DBD) reactors for ozone generation in atmospheric air*. PhD Thesis, University of Florida, 2018.
13. Yu YH, Gmelin B, Splettstoesser W, et al. Reduction of helicopter blade-vortex interaction noise by active rotor control technology. *Prog Aerospace Sci* 1997; 33(9–10): 647–687. DOI: 10.1016/S0376-0421(97)00006-7.
14. Charles BD, Hassan AA, Tadghighi H, et al. Blade vortex interaction noise reduction techniques for a rotorcraft. US Patent No. 5,588,800, 1996.
15. Schmitz FH. Reduction of blade-vortex interaction (BVI) noise through X-Force Control. *J Am Helicopter Soc* 1998; 43(1): 14–24. DOI: 10.4050/JAHS.43.14.
16. Hardin JC and Lamkin SL. Concepts for reduction of blade/vortex interaction noise. *J Aircraft* 1987; 24(2): 120–125. DOI: 10.2514/3.45428.
17. Charles BD, Hassan AA, Tadghighi H, et al. Tapered/segmented flaps for rotor blade-vortex interaction (BVI) noise and vibration reduction. US Patent No. 6,478,541 B1, 2002.
18. Lee S. Reduction of blade-vortex interaction noise through porous leading edge. *AIAA J* 1994; 32(3): 480–488. DOI: 10.2514/3.12011.
19. Malpica C, Greenwood E and Sim BWC. Helicopter Non-Unique Trim Strategies for Blade-Vortex Interaction (BVI) Noise Reduction. In: AHS Specialists' Conference on Aeromechanics Design for Vertical Lift of the American Helicopter Society, pp. 485–493. 20-22 January, 2016, San Francisco, CA.
20. Chen PC, Baeder JD, Evans RAD, et al. Blade-vortex interaction noise reduction with active twist smart rotor technology. *Smart Mater Structures* 2001; 10(1): 77–85. DOI: 10.1088/0964-1726/10/1/307.
21. Brooks TF, Booth ER, Jolly JR, et al. Technical notes: reduction of blade-vortex interaction noise through higher harmonic pitch control. *J Am Helicopter Soc* 1990; 35(1): 86–91. DOI: 10.4050/JAHS.35.86.

22. Baeder JD and Sim BWC. Blade-Vortex Interaction Noise Reduction by Active Trailing-Edge Flaps. In: 54th Annual Forum of the American Helicopter Society. 20-22 May, 1998, Washington, DC.
23. Yu YH. Miss distance for rotor blade-vortex interaction noise reduction. In: 2nd AIAA/CEAS Aeroacoustics Conference, AIAA Paper No. 96-1738, p. 14. 6-8 May, 1996, State College, PA, DOI: 10.2514/6.1996-1738.
24. Malpica C, Greenwood E and Sim BWC. Parametric investigation of the effect of hub pitching moment on blade vortex interaction (BVI) noise of an isolated rotor. In: 72nd annual forum proceedings of the American Helicopter Society, 17-19 May, 2016, West Palm Beach, FL, pp. 188–201.
25. Romani G and Casalino D. Rotorcraft blade-vortex interaction noise prediction using the Lattice-Boltzmann method. *Aerospace Sci Technol* 2019; 88: 147–157. DOI: 10.1016/j.ast.2019.03.029.
26. Xue Y and Lyrintzis AS. Rotating Kirchhoff method for three-dimensional transonic blade-vortex interaction hover noise. *AIAA J* 1994; 32(7): 1350–1359. DOI: 10.2514/3.12202.
27. Caradonna F, Kitaplioglu C, McCluer M, et al. Methods for the prediction of blade-vortex interaction noise. *J Am Helicopter Soc* 2000; 45(4): 303–317. DOI: 10.4050/JAHS.45.303.
28. Glegg SAL. Prediction of blade wake interaction noise based on a turbulent vortex model. *AIAA J* 1991; 29(10): 1545–1551. DOI: 10.2514/3.10774.
29. Beaumier P, Prieur J, Spiegel P, et al. Effect of higher harmonic control on helicopter rotor blade-vortex interaction noise: prediction and initial validation. In: 75th Fluid Dynamics Symposium AGARD Conference Proceedings, 10-13 October, 1994, Berlin, Germany, pp. 26–31.
30. Zhao Y, Shi Y and Xu G. Helicopter blade-vortex interaction airload and noise prediction using coupling CFD/VWM method. *Appl Sci* 2017; 7(4): 381. DOI: 10.3390/app7040381.
31. Rahier G and Delrieux Y. Blade-vortex interaction noise prediction using a rotor wake roll-up model. *J Aircraft* 1997; 34(4): 522–530. DOI: 10.2514/2.2204.
32. Spiegel P, Rahier G and Michéa B. Blade-vortex interaction noise–prediction and comparison with flight and wind tunnel tests. Technical report, ONERA TP No, 1992-126, 1992.
33. Chung KH, Hwang CJ, Jeon W, et al. Blade vortex interaction noise prediction of the isolated rotor of a helicopter. In: The 9th Western Pacific Acoustics Conference, Seoul, Korea, 26 June–28 June 2006.WESPAC IX.
34. Tangler JL. Schlieren and noise studies of rotors in forward flight. In: 33rd Annual National Forum of the American helicopter society. 9 May, 1977, Washington, DC, pp. 33–05.
35. Straub FK, Anand VR, Lau BH, et al. Wind tunnel test of the SMART active flap rotor. *J Am Helicopter Soc* 2018; 63(1): 1–16. DOI: 10.4050/JAHS.63.012002.
36. Huang X and Zhang X. Streamwise and spanwise plasma actuators for flow-induced cavity noise control. *Phys Fluids* 2008; 20(3): 037101. DOI: 10.1063/1.2890448.
37. Thomas FO, Kozlov A and Corke TC. Plasma actuators for cylinder flow control and noise reduction. *AIAA J* 2008; 46(8): 1921–1931. DOI: 10.2514/1.27821.
38. Huang X, Zhang X and Li Y. Broadband flow-induced sound control using plasma actuators. *J Sound Vibration* 2010; 329(13): 2477–2489. DOI: 10.1016/j.jsv.2010.01.018.
39. Al-Sadawi L, Chong TP and Kim JH. Aerodynamic noise reduction by plasma actuators for a flat plate with blunt trailing edge. *J Sound Vibration* 2019; 439: 173–193. DOI: 10.1016/j.jsv.2018.08.029.
40. Riherd M and Roy S. Serpentine geometry plasma actuators for flow control. *J Appl Phys* 2013; 114(8): 083303. DOI: 10.1063/1.4818622.
41. Roy S, Zhao P, DasGupta A, et al. Dielectric barrier discharge actuator for vehicle drag reduction at highway speeds. *AIP Adv* 2016; 6(2): 025322. DOI: 10.1063/1.4942979.
42. Roy S. Devices employing one or more plasma Actuators. US Patent No 9,769,914 B2, 2017.
43. Greenwood E, Schmitz FH and Sickenberger RD. A semiempirical noise modeling method for helicopter maneuvering flight operations. *J Am Helicopter Soc* 2015; 60(2): 1–13. DOI: 10.4050/JAHS.60.022007.

44. Greenwood E and Schmitz FH. A parameter identification method for helicopter noise source identification and physics-based semiempirical modeling. *J Am Helicopter Soc* 2018; 63(3): 1–14. DOI: 10.4050/JAHS.63.032001.
45. Boxwell DA and Schmitz FH. Full-scale measurements of blade-vortex interaction noise. *J Am Helicopter Soc* 1982; 27(4): 11–27. DOI: 10.4050/JAHS.27.4.11.
46. Moore DW and Saffman PG. Axial flow in laminar trailing vortices. *Proc R Soc Lond A Math Phys Sci* 1973; 333(1595): 491–508. DOI: 10.1098/rspa.1973.0075.
47. McCormick BW. *Aerodynamics of V/STOL Flight*. Mineola, NY: Dover Publications, 1999.
48. Ffowcs Williams JE and Hawkings DL. Sound generation by turbulence and surfaces in arbitrary motion. *Philos Trans R Soc A Math Phys Eng Sci* 1969; 264(1151): 321–342. DOI: 10.1098/rsta.1969.0031.
49. Thielicke W and Stamhuis EJ. PIVlab–Towards user-friendly, affordable and accurate digital particle image velocimetry in MATLAB. *J Open Res Softw* 2014; 2: e30. DOI: 10.5334/jors.bl.
50. ANSYS FLUENT. Academic Research Release, 2020.
51. Carlson JR. Inflow/outflow boundary conditions with application to FUN3D. NASA/TM, 2011;217181.
52. Singh KP and Roy S. Force approximation for a plasma actuator operating in atmospheric air. *J Appl Phys* 2008; 103(1): 013305. DOI: 10.1063/1.2827484.
53. Benard N and Moreau E. Electrical and mechanical characteristics of surface ac dielectric barrier discharge plasma actuators applied to airflow control. *Exp Fluids* 2014; 55(1846): 1–43. DOI: 10.1007/s00348-014-1846-x.
54. Victor Kopiev V, Faranosov G, Bychkov O, et al. Active control of jet-plate interaction noise for excited jets by plasma actuators. *J Sound Vibration* 2020; 484: 115515. DOI: 10.1016/j.jsv.2020.115515.
55. Landgrebe AJ. The wake geometry of a hovering helicopter rotor and its influence on rotor performance. *J Am Helicopter Soc* 1972; 17(4): 3–15. DOI: 10.4050/JAHS.17.4.3.
56. Beddoes TS. Practical computation of lift. In: Eighth European rotorcraft forum. Aix-En-Provence, France. 31 August–3 September, 1982.
57. Vatistas GH, Kozel V and Mih WC. A simpler model for concentrated vortices. *Experiments in Fluids* 1991; 11(1): 73–76. DOI: 10.1007/BF00198434.
58. Brentner KS and Farassat F. Modeling aerodynamically generated sound of helicopter rotors. *Prog Aerospace Sci* 2003; 39(2–3): 83–120. DOI: 10.1016/S0376-0421(02)00068-4.
59. Ladson CL. Effects of independent variation of mach and reynolds numbers on the low-speed aerodynamic characteristics of the NACA 0012 airfoil section. NASA-TM, 1988; 4074.
60. Schmitz FH and Yu YH. Helicopter Impulsive Noise: Theoretical and Experimental Status. In: *Recent advances in aeroacoustics, chapter 6*. New York, NY: Springer; 1986, pp. 149–243. DOI: 10.1007/978-1-4612-4840-8́6.